Proceedings of the Royal Society A: Mathematical, Physical and Engineering Sciences,
2017, Vol. 473, Iss. 2200, article number 20160672
DOI:10.1098/rspa.2016.0672

Flow through a very porous obstacle in a shallow channel

M. Creed[1], S. Draper[2], T. Nishino[3] and A. G. L. Borthwick[1]

[1]Institute for Energy Systems, School of Engineering, Univ. of Edinburgh, The King's Buildings, Edinburgh EH9 3JL, U.K.

[2]School of Civil, Environmental and Mining Engineering, University of Western Australia, WA 6009, Australia

[3]Centre for Offshore Renewable Energy Engineering, Cranfield University, Bedfordshire MK43 0AL, UK

A theoretical model, informed by numerical simulations based on the shallow-water equations, is developed to predict the flow passing through and around a uniform porous obstacle in a shallow channel, where background friction is important. This problem is relevant to a number of practical situations, including flow through aquatic vegetation, the performance of arrays of turbines in tidal channels, and hydrodynamic forces on offshore structures. To demonstrate this relevance, the theoretical model is used to (i) reinterpret core flow velocities in existing laboratory-based data for an array of emergent cylinders in shallow water emulating aquatic vegetation, and (ii) reassess the optimum arrangement of tidal turbines to generate power in a tidal channel. Comparison with laboratory-based data indicates a maximum obstacle resistance (or minimum porosity) for which the present theoretical model is valid. When the obstacle resistance is above this threshold the shallow water equations do not provide an adequate representation of the flow, and the theoretical model over-predicts the core flow passing through the obstacle. The second application of the model confirms that natural bed resistance increases the power extraction potential for a partial tidal fence in a shallow channel and alters the optimum arrangement of turbines within the fence.

1. Introduction

Shallow flow through a porous obstacle is commonly encountered in environmental fluid mechanics; examples include: flow in aquatic vegetation such as reeds and coastal or river bed vegetation (Zong and Nepf, 2011; Chen *et al.* 2012); flow through a group of offshore pile foundations (Ball *et al.*, 1996); flow through a tidal stream turbine or array of turbines (Garrett and Cummins, 2007, 2013); and urban flood flows, where the porous obstacle could represent a group of buildings (Soares-Frazão *et al*. 2010). In all of these scenarios it is important to estimate how changes in the porosity of the obstacle, and therefore changes in the obstacle's net resistance, will alter the velocity of the core flow passing through it. This is because the core flow velocity influences directly the hydrodynamic forces experienced by the constituent structures within the obstacle, as well as the flow structure in the wake of the obstacle.

In general, a shallow water flow must divert around an obstacle as its porosity reduces. However, in any realistic scenario the functional relationship between porosity and the core flow velocity will be influenced by additional factors that inhibit or encourage flow diversion. Two common factors include natural bed resistance in the channel (which essentially defines the relative resistance of the obstacle) and lateral flow confinement (which provides a geometric restriction on flow diversion when the channel is narrow relative to the obstacle width). A simple but practically relevant problem which incorporates these two factors is that of a uniformly porous obstruction extending through the full water depth in a shallow channel (figure 1). In this problem the obstacle, represented as a patch of increased bed friction, is located in the centre of the channel and is assumed to be rectangular, with planar dimensions w and l, and compact, such that the aspect ratio $A_R = w/l \geq 1$. The channel is assumed to have uniform depth h_0, width W, and uniform flow with steady depth-averaged upstream velocity U. Natural bed resistance is introduced as a quadratic drag coefficient C_d, and the resistance of the obstruction is defined in terms of the net drag of the individual constituent structures within the obstacle.

©2017. The Royal Society. This is the Author Accepted Manuscript.
Please refer to any applicable publisher terms of use.

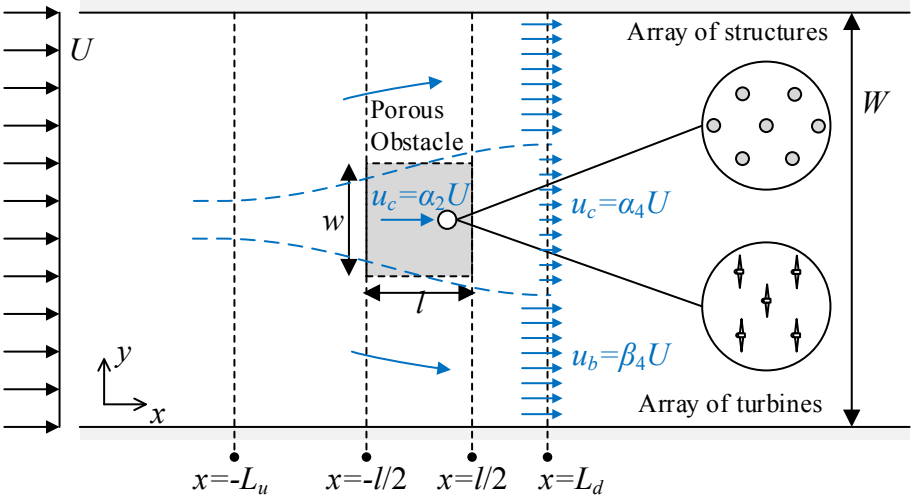

Figure 1: Top view of a channel with a porous obstacle extending through the water column. Symbols and locations defined in §4.

Provided that h_0 is small (i.e. shallow) relative to the obstacle and channel dimensions, the usual approach is to use the shallow water equations to model this type of simplified problem. If the Froude number is small, it is then possible to show that three dimensionless parameters influence the core flow velocity, provided the obstacle is compact (i.e. A_R>~1; see §3). These parameters are: (i) the porosity of the obstacle (or, equally, its dimensionless resistance k); (ii) $S = C_d w/h_0$, which explains the importance of natural drag and is often referred to as a wake stability number in the literature on shallow flow (Chen and Jirka, 1995); and (iii) the channel blockage ratio $B = w/W$. Collectively this set of three parameters defines a parameter space in which to explore the core flow passing through the obstacle, with the solution space having direct application to problems related to aquatic vegetation, offshore structures, and tidal turbine arrays. To date however, previous studies have only explored parts of the parameter space for this simplified problem, focusing on just one parameter (porosity) or two parameters (porosity and stability number or channel blockage ratio). For example, Chen and Jirka (1995), Chen *et al.* (2012), Zong and Nepf (2011), Takemura and Tanaka (2007), and Ball *et al.* (1996), among others, have conducted laboratory experiments of shallow flow around different arrangements of emergent rigid cylinders representing a porous obstacle in a channel, whilst Nicolle and Eames (2011) carried out 2D numerical simulations of flow through a circular arrangement of rigid cylinders. In these works, the flow field and the shallow wake were investigated for different cylinder spacing (i.e. different obstacle porosity) but the effects of both stability number and channel blockage ratio were not systematically explored.

In contrast to the foregoing experimental work on cylinder arrays, most theoretical work concerning arrays of tidal stream turbines has focused on the effect of channel blockage ratio on core flow velocity and, in turn, the power dissipated by a porous obstacle representing a single turbine or a row/array of turbines (e.g. Garrett and Cummins, 2007; Houlsby *et al.* 2008; Nishino and Willden, 2012; Draper and Nishino, 2014). These studies of tidal stream turbine arrays have applied control volume arguments to the problem in figure 1, and have demonstrated that for a given obstacle resistance the core flow velocity and power extraction increases with blockage ratio; i.e. blockage is advantageous from the perspective of tidal power generation. However the majority of these studies are restricted to the assumption $S = 0$; the one exception being Garrett and Cummins (2013), who investigate the power that can be removed by a tidal turbine farm modelled as a circular patch in a frictional flow, but under the opposite restriction that B~0.

Motivated by this earlier body of work, the aim of the present paper is to explore the solution for the depth-averaged core flow velocity passing through the porous obstacle represented in figure 1, accounting for the combined influence of porosity, channel blockage, and natural friction. To achieve this, an approximate theoretical model has been developed which extends conventional momentum theory for a porous obstacle in a finite channel to include background bed friction. It is shown that the inclusion of background friction introduces an additional unknown length scale. To close the theoretical model, numerical solutions of the shallow water equations have therefore been used to estimate this length scale over a practical range of S, B and k. To demonstrate the utility of the new theoretical model, it is then applied to two outstanding problems: firstly, the prediction of the flow through a very porous patch of aquatic vegetation; and secondly, the optimum arrangement of tidal turbines within a shallow tidal channel.

The theoretical model presented in this paper, and the numerical simulations performed to close the model, assume that depth-averaged shallow water equations are a satisfactory approximation to the flow field. With respect to this assumption, Stansby (2006) has described limitations to depth-averaged modelling in the near wake of a solid body in shallow water. Specifically, it has been shown that changes in velocity gradients and shear stresses near the bed, which result from horizontal and vertical mixing in the wake of the body, cannot be captured in a depth-averaged model (Stansby, 2003). This implies that a shallow water model may not capture the amplification in bed shear stress in the near wake of a solid body. Since this shear stress would act to resist flow through a porous obstacle, it also implies that a shallow water model is expected to over-predict the core flow velocity passing through the porous obstacle. In addition, Ball *et al.* (1996) found that an artificially high pile drag coefficient was required in shallow water numerical simulations to match the measured velocity profiles from experiments of flow through a group of piles. Ball *et al.* also showed that the ratio of the numerical drag coefficient (required to match the measured velocity) to the experimental drag coefficient increased as the porosity of the pile group decreased. In light of these earlier studies, the shallow water equations are used in this paper on the assumption that mixing and associated amplification of bed shear stress in the near wake of the obstacle are small. Comparison of the model results with experiments in §5.1 indicates the minimum obstacle porosities (maximum obstacle resistance) for which this assumption appears to be valid.

2. Theoretical model

To develop an approximate theoretical model for the problem in figure 1, a general form of the flow field is first assumed, and then arguments involving mass, energy and momentum conservation are used to relate the core flow velocity to the obstacle resistance in a similar way to that demonstrated by Garrett and Cummins (2007) for an obstacle in a frictionless channel.

Figure 1 illustrates the assumed flow field, which has two key features. Firstly, the depth-averaged core and bypass flows, which are delineated by the dashed streamlines, are assumed to be uniform (i.e. one dimensional). Secondly, the dividing streamlines are drawn as smoothly diverging lines, which implies that the depth-averaged core flow velocity $u_c(x)$ and the depth-averaged bypass velocity $u_b(x)$ vary smoothly and monotonically along the channel. Specifically, the core flow velocity reduces from the free stream velocity to $\alpha_2 U$ at the centre of the obstacle, before reducing further to a minimum velocity $\alpha_4 U$ in the near wake of the obstacle. Invoking continuity, the bypass flow velocity increases from the free stream velocity to a maximum velocity $\beta_4 U$ when the core flow is a minimum. The length scale over which these changes in core and bypass velocity take place is $L = L_u + L_d$, where L_u and L_d are the distances upstream and downstream of the obstacle where streamlines are close to parallel. Hence L_u is an upstream adjustment length using the terminology of Rominger and Nepf (2011), and L_d defines the distance from the centre of the obstacle to the near wake. The smooth variations in core and

bypass flow velocities over these length scales are approximated by a cubic spline (as outlined in the Appendix); we show later in §3 that the use of a cubic spline agrees well with numerical simulations and laboratory based data for the core flow.

Based on the above description of the flow field it is possible to relate the velocity coefficients in the core and bypass flow to the obstacle resistance using conservation arguments. First, continuity is used to write $\alpha_4 Uw(\alpha_2/\alpha_4) + \beta_4 Uw(1/B - \alpha_2/\alpha_4) = UW$, so that

$$\alpha_2 = \frac{\alpha_4(1-\beta_4)}{B(\alpha_4-\beta_4)}. \tag{2.1}$$

Next, the Bernoulli equation is written along any streamline passing through the obstacle. Undertaking this separately upstream and downstream of the obstacle, and taking the difference, gives

$$p_{-l/2} - p_{l/2} = p_{-L_u} - p_{L_d} + \frac{1}{2}\rho U^2(1-\alpha_4^2) - \rho S \int_{-L_u/w}^{L_d/w} u_c^2 \ \mathrm{d}(x/w), \tag{2.2}$$

where ρ is the fluid density and the last term in (2.2) accounts for losses due to bed friction over the upstream and downstream regions of the core flow, respectively, and p_{x_i} represents the pressure at different locations x_i along the channel (noting that p is equal to ρg times the free surface elevation). Strictly speaking the integral in (2.2) should omit the region within the obstacle; however it is assumed that this region is small compared to L when $A_R >1$.

The Bernoulli equation can also be written along a streamline in the bypass flow, leading to

$$p_{-L_u} - p_{L_d} = \frac{1}{2}\rho U^2(\beta_4^2 - 1) + \rho S \int_{-L_u/w}^{L_d/w} u_b^2 \ \mathrm{d}(x/w). \tag{2.3}$$

Combining (2.3) with (2.2) gives

$$p_{-l/2} - p_{l/2} = \frac{1}{2}\rho U^2(\beta_4^2 - \alpha_4^2) + \rho S \int_{-L_u/w}^{L_d/w} (u_b^2 - u_c^2) \ \mathrm{d}(x/w). \tag{2.4}$$

Finally, writing a streamwise momentum balance for the channel extending between $x = -L_u$ and $x = L_d$ leads to

$$\begin{aligned} &\frac{wh_0}{B}(p_{-L_u} - p_{L_d}) - T - F_b - F_c \\ &\qquad = \rho U^2 \alpha_2 w h_0(\alpha_4 - 1) + \rho U^2\left(\frac{1}{B} - \alpha_2\right) w h_0(\beta_4 - 1), \end{aligned} \tag{2.5}$$

where T is the total retarding force component due to the obstacle, and F_b and F_c are force components associated with seabed friction in the bypass flow and core flow, respectively, given by

$$F_b = \rho C_d U^2 w L\left(\frac{w}{L}\right) \int_{-L_u/w}^{L_d/w} \frac{w_b}{w}\left(\frac{u_b}{U}\right)^2 \mathrm{d}(x/w) \quad \text{and} \quad F_c = \rho C_d U^2 w L\left(\frac{w}{L}\right) \int_{-L_u/w}^{L_d/w} \frac{w_c}{w}\left(\frac{u_c}{U}\right)^2 \mathrm{d}(x/w), \tag{2.6}$$

where w_b and w_c are the width of the by-pass flow and core flow, respectively (see Appendix). In (2.5) we have assumed that the change in water elevation upstream and downstream of the obstacle is small so that the difference in hydrostatic pressure integrated across the channel cross section at $x = -L_u$ and $x = L_d$ is given approximately as $wh_0(p_{-L_U} - p_{L_d})/B$. The change in water elevation will be small provided that the Froude number is small (see Garrett and Cummins, 2007).

Noting that $T = \left(p_{-l/2} - p_{l/2}\right)wh_0$, it follows that (2.6) can be combined with (2.1) and (2.5) to give

$$\beta_4^2(1-B) - \beta_4(2-2\alpha_4) + (1-2\alpha_4+\alpha_4^2 B) + SX = 0, \tag{2.7}$$

with

$$X = 2\int_{-L_u/w}^{L_d/w}\left(\frac{u_b}{U}\right)^2 \mathrm{d}(x/w) - 2B\int_{-L_u/w}^{L_d/w}\left\{\left(\frac{u_b}{U}\right)^2 - \left(\frac{u_c}{U}\right)^2 + \frac{w_b}{w}\left(\frac{u_b}{U}\right)^2 + \frac{w_c}{w}\left(\frac{u_c}{U}\right)^2\right\}\mathrm{d}(x/w). \tag{2.8}$$

To complete the analysis, it is also possible to write, from (2.5) and (2.4), that

$$\frac{T}{\frac{1}{2}\rho U^2 w h_0} = k\alpha_2^2 = (\beta_4^2 - \alpha_4^2) + 2S\int_{-L_u/w}^{L_d/w}\frac{(u_b^2 - u_c^2)}{U^2}\mathrm{d}(x/w). \tag{2.9}$$

where k represents a local drag coefficient which, as noted in the Introduction, may be interpreted as the dimensionless resistance of the obstacle.

Equations (2.1), (2.7) and (2.9) now provide the relationships that link the obstacle resistance to the core flow velocity. For example, by selecting values for *S, B,* $L_u' = L_u/w$ and $L_d' = L_d/w$ for a given scenario, it is possible to choose a wake velocity coefficient α_4 and simultaneously solve (2.7) for β_4 and either (2.1) or (2.5) for α_2 numerically. Finally, since the resistance k corresponding to the chosen α_4 can be determined from (2.9) it is possible to obtain the core flow velocity in the functional form: $\alpha_2(k, B, S, L_u', L_d')$.

The solution can be obtained numerically and gives an identical result to that obtained by Garrett and Cummins (2007) when $S = 0$. Alternatively, when $S > 0$ the only practical difficulty in using the model is that the length scales L_u' and L_d' must be quantified. Accurate evaluation of these length scales is difficult because, although scaling arguments may be useful in some scenarios (i.e. Rominger and Nepf, 2011, use scaling arguments to suggest that $L_u \sim O(w/2)$ when $B \approx 0$), in general L_u' and L_d' may vary with changes in blockage ratio and additional parameters such as the stability number. To explore this dependency numerical simulations are employed in the following section.

3. Numerical Simulations

3.1 Shallow Water Model

The depth-averaged continuity and momentum equations may be used to approximate the flow through the channel in figure 1. These are given by

$$\frac{\partial h}{\partial t} + \nabla\cdot(h\mathbf{u}) = 0, \tag{3.1}$$

$$\rho h\frac{\partial \mathbf{u}}{\partial t} + \rho h(\mathbf{u}\cdot\nabla)\mathbf{u} = -\rho g h\nabla h - \rho\left(C_d + C_p\right)\mathbf{u}|\mathbf{u}|\,, \tag{3.2}$$

where $\mathbf{u} = (u, v)$ represents the depth-averaged velocity vector in horizontal Cartesian coordinates (x, y), t is time, g is the acceleration due to gravity, ρ is the density of the fluid, h is water depth, C_d parameterises natural bed resistance throughout the channel, and C_p parameterises the (additional) equivalent shear stress τ_p due to the porous obstacle (and is non-zero only within the obstacle); so that,

$$\tau_p = \rho C_p u|u|. \tag{3.3}$$

Depending on the application, (3.3) may be rewritten in terms of the drag coefficients, and the dimensions and solid volume fraction of constituent structures within the obstacle. For an array of

emergent circular cylinders, the depth-averaged force per unit plan area may be estimated as (Rominger and Nepf, 2011)

$$\tau_p = \frac{n\left(\frac{1}{2}\rho c_D (d h_0) u|u|\right)}{1-\phi}, \tag{3.4}$$

where c_D is the local drag coefficient of an individual cylinder, d is the cylinder diameter, n is the number of cylinders per unit plan area of the obstacle and $\phi = \pi n d^2/4$ is the solid volume fraction of cylinders within the obstacle (*i.e.* the geometric porosity is equal to $1-\phi$). It should be noted that (3.4) is only an approximation of the total force if c_D is chosen based on data for isolated cylinders. A more accurate estimate would include an effective c_D accounting for interference effects between cylinders.

Alternatively, for an array of tidal stream turbines the net force per unit width perpendicular to the flow is usually expressed in terms of the resistance k (Draper and Nishino, 2014); i.e.

$$F = \tau_p l = \frac{1}{2}\rho k h_0 u|u|. \tag{3.5}$$

Equating forces therefore gives

$$k = \frac{2C_p l}{h_0} = \frac{c_D a l}{1-\phi} = \frac{4 c_D \phi l}{\pi d (1-\phi)}. \tag{3.6}$$

where $a = nd$ is the frontal area of cylinders per unit volume (Rominger and Nepf, 2011). Hence k may be used to represent the resistance of an array of turbines or an array of cylindrical structures. Throughout this paper resistance of the obstacle is therefore presented in terms of k, although conversion to alternative parameters is straightforward using (3.6).

To simplify the problem it is useful to introduce non-dimensional variables $h' = h/h_0$, $\mathbf{x}' = \mathbf{x}/w$, $\mathbf{u}' = \mathbf{u}/U$ and $t' = tU/w$. Equations (3.1) and (3.2) then become

$$\frac{\partial h'}{\partial t'} + \nabla \cdot (h'\mathbf{u}') = 0, \tag{3.7}$$

$$h'\frac{\partial \mathbf{u}'}{\partial t'} + h'(\mathbf{u}'\cdot\nabla)\mathbf{u}' = -\frac{1}{Fr^2} h' \nabla h' - \left(S + \frac{1}{2} k A_R\right)\mathbf{u}'|\mathbf{u}'|, \tag{3.8}$$

where $Fr = U/\sqrt{g h_0}$ is the Froude number of the upstream uniform flow and, as defined in the Introduction, $S = C_d w/h_0$ is the stability number and $A_R = w/l$ is the aspect ratio of the obstacle. Scaling the geometry in figure 1 introduces an additional non-dimensional parameter: $B = w/W$. Hence, together with the obstacle resistance k, and the three parameters; *S, B* and A_R, a total of five parameters enter the problem. This set can be reduced to three if it is assumed that (i) Fr is small, so that variations in water depth are everywhere small (i.e. $\nabla h'$ is small), and (ii) the aspect ratio is of secondary importance for a compact obstacle (which we show to be the case in §3.2). Consequently, the dimensionless velocity field and the length scales $L_u^{'}$ and $L_d^{'}$ will depend only on the obstacle resistance k, the stability number *S* and the channel blockage ratio *B*.

3.2 Numerical solution

Equations (3.7) and (3.8) are solved numerically using a finite-volume Godunov-type HLLC Riemann solver (Toro *et al.*, 1994) with MUSCL Hancock time integration to ensure second-order accuracy in time and space. Free slip solid wall, reflective boundary conditions are applied at the channel side walls, whilst at the upstream boundary the discharge is prescribed and the water depth is extrapolated from cells inside the domain. The water depth is fixed at the downstream boundary and the discharge is free to vary by extrapolation. Domain boundaries are located $6w$ upstream and $25w$ downstream of

the obstacle to ensure that upstream flow divergence and downstream wake formation are not influenced by these boundaries. The obstacle is inserted into the channel at $t = 0$ and the numerical model is run until the local flow field close to the obstacle is approximately steady. For low values of stability number this local flow field is not exactly steady, due to the development of vortices in the far downstream wake flow field. The formation of these vortices is qualitatively similar to that for a bluff body with base bleed (Wood, 1964), but only results in small fluctuations (approximately 1-2%) in the velocity of the core flow passing through the obstacle.

A uniform grid of square elements is used in the simulations. The time step is chosen to give a maximum Courant-Friedrichs-Lewy number of 0.9. Grid convergence tests indicate that with this time step changes in bulk flow velocity are generally less than 1% when the number of grid cells was doubled from 32 to 64 across the width of the obstacle. A mesh with 32 cells/w is therefore used throughout. Numerical simulations are conducted over the finite parameter space $S \times B = (0, 0.09, 0.5, 1.0, 1.5) \times (0.05, 0.1, 0.25, 0.32, 0.5)$, which is a representative range for aquatic vegetation, offshore structures, and tidal turbine arrays. For each combination of S and B within this space, a minimum of 4 to 6 different k values were investigated, ranging from $k = 1$ to $k = 12 - 60$, depending on stability number and blockage ratio. This range is adequate to identify the maximum power dissipated by the obstacle for tidal turbine applications. It also provides a range of obstacle resistance values typical of aquatic vegetation such as kelp forests or mangrove forests, the latter which can be very dense and have large associated k values (see for example, Jackson, 1997, Mazda *et al.*, 1997). In all simulations $Fr = 0.05$, which was found to be a sufficiently small value that the flow was insensitive to any further reduction in Fr.

Preliminary simulations have also considered different obstacle aspect ratios (see Table 1). However, when k is fixed, the influence of this ratio on the core flow velocity is found to be negligible at low stability number, whilst at larger stability number ($S > 0.5$) the core flow velocity is only sensitive to aspect ratio if the aspect ratio is small ($A_R < 2$). This lack of sensitivity to aspect ratio for sufficiently compact obstacles implies that the flow does not 'feel' the length of a compact obstacle, and so cannot differentiate between the different aspect ratios modelled. Instead, the flow is resisted only by the net force applied by the obstacle, which is described entirely by k irrespective of obstacle length. This result verifies the assumption made in §2, equation (2.2), that the region within the obstacle can be included in the integral without affecting the overall result, provided that $A_R > 1$. For convenience, a value of $A_R = 4$ is adopted throughout the remaining numerical simulations presented in this paper so that the results are representative of a compact obstacle (i.e. with $A_R > 1$) over the range of k, S and B values investigated.

	$\boldsymbol{A_R}$ =1	$\boldsymbol{A_R}$ =2	$\boldsymbol{A_R}$ =4	$\boldsymbol{A_R}$ =8	$\boldsymbol{A_R}$ =16	$\boldsymbol{A_R}$ =32
$S = 0$	0.538	0.532	0.526	0.525	0.523	0.522
$S = 0.2$	0.553	0.546	0.537	0.531	0.530	0.528
$S = 0.5$	0.618	0.599	0.585	0.577	0.573	0.573
$S = 1.5$	0.730	0.694	0.671	0.659	0.652	0.649

Table 1. Core flow velocity parameter $\boldsymbol{\alpha_2}$ (defined in equation (3.9)) for $\boldsymbol{B}$ = 0.5, $\boldsymbol{k}$ = 12.

3.3 Numerical results

Figure 2 presents the computed depth-averaged velocity field for two example blockage ratios ($B =$ 0.05 and 0.5) and three example stability numbers ($S = 0$, 0.09 and 0.5) when the obstacle has a fixed

resistance of $k = 12$. For comparison, the figures also show the two streamlines which bound the fluid passing through the centre of the obstacle. It can be seen that these streamlines diverge upstream of the obstacle, as the core flow velocity reduces. Downstream of the obstacle the streamlines then continue to diverge. For $S > 0$, the quadratic background friction preferentially slows the faster bypassing flow so that both the bypass and wake flow speeds recover to those of the upstream flow, and the streamlines begin to converge.

Across the different scenarios in figure 2 it can be seen that the streamlines which bound the flow passing through the obstacle diverge by a greater amount when both the blockage ratio and stability number are small; indicating a larger reduction in core flow velocity for low stability number and low blockage ratio. The reduction in core flow velocity is illustrated in more detail in figure 3, which presents normalised core flow velocity along $y/w = 0$. Figure 3 also illustrates that the core flow velocity begins to reduce over some adjustment length upstream of the obstacle, and then continues to reduce monotonically through the obstacle (with a reduction that is well approximated by the simple cubic spline functions given in the Appendix) before becoming constant or increasing at some distance beyond the near wake of the obstacle. Variations in the adjustment length, and the overall profile of the core flow velocity along the channel in figure 3, can be seen to be mostly due to changes in the stability number and blockage ratio. In contrast, only very minor differences are evident across the range in resistance k that have been investigated.

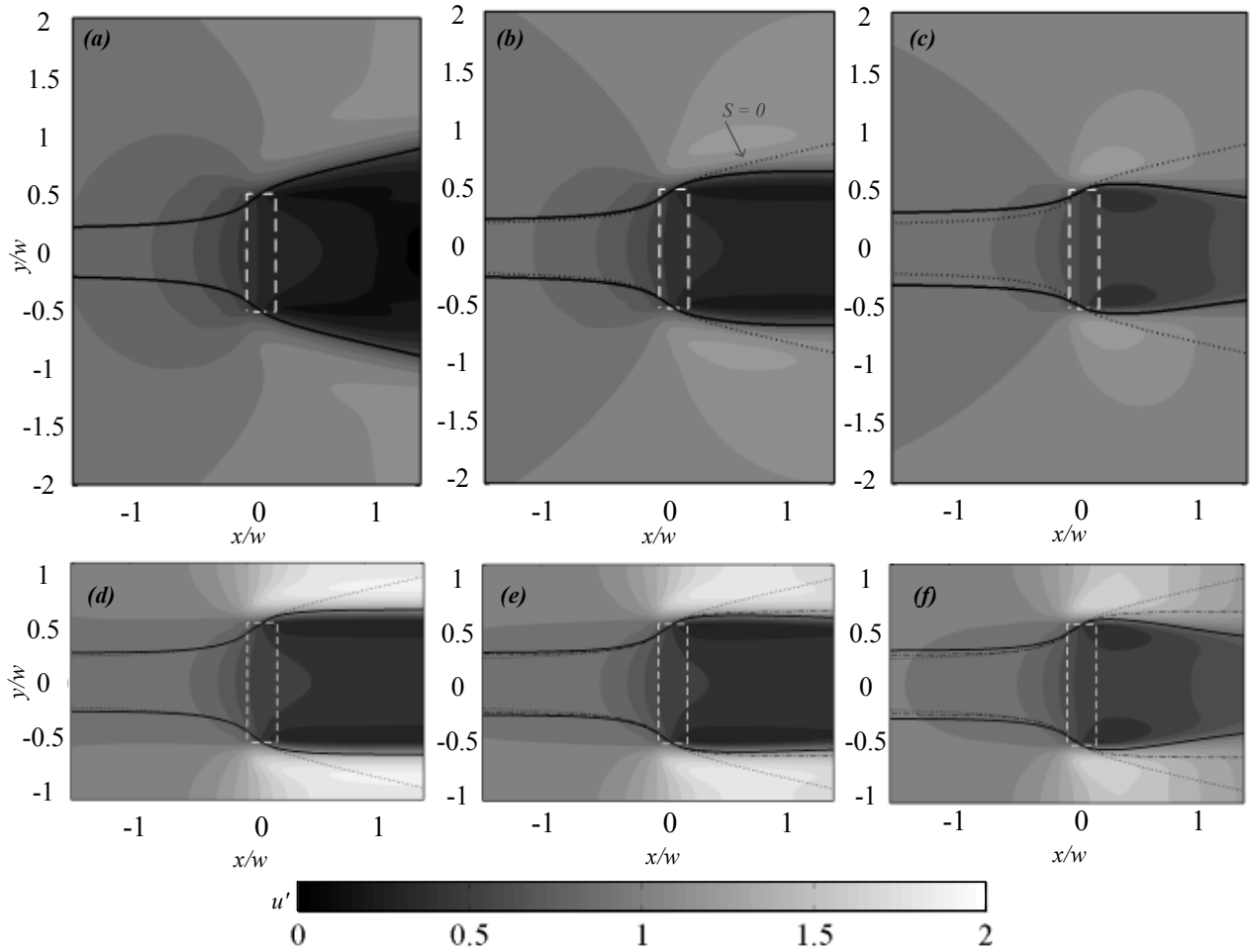

Figure 2. Contours of u' for *(a)* $S = 0, B = 0.05$; *(b)* $S = 0.09, B = 0.05$; *(c)* $S = 0.5, B = 0.05$; *(d)* $S = 0, B = 0.5$; *(e)* $S = 0.09, B = 0.5$ and *(f)* $S = 0.5, B = 0.5$. Solid lines indicate streamlines bounding flow through the centre of the obstacle, dash-dot lines indicate the corresponding streamlines for $S = 0$ and the same blockage ratio, and dotted lines indicate the streamlines for $S = 0, B = 0.05$. Dashed line represents the obstacle outline. $A_R = 4$, $k = 12$.

When developing the theoretical model in §2, two important assumptions were made regarding the flow field. Firstly, it was assumed that the core and bypass flows are uniform. Secondly it was assumed that the core and bypass flow velocities vary smoothly and monotonically along the channel. The second of these assumptions is consistent with figure 3 in that the core velocity reduces gradually upstream and continues to decrease within, and immediately downstream of, the obstacle. With respect to the first assumption, it can be seen in figure 2 that at the higher blockage ratio (i.e. $B = 0.5$) and low stability number (i.e. $S \leq 0.09$), the increase in velocity is close to uniform across the bypass flow, which is in good agreement with the model. However, for larger stability number (and especially when the blockage ratio is small) the increase in bypass velocity becomes more confined to a region close to the obstacle; hence the bypass flow becomes increasingly two-dimensional as both the stability number increases and the blockage ratio reduces. Consequently, the theoretical model assumptions become less representative for these scenarios, as seen in figure 3.

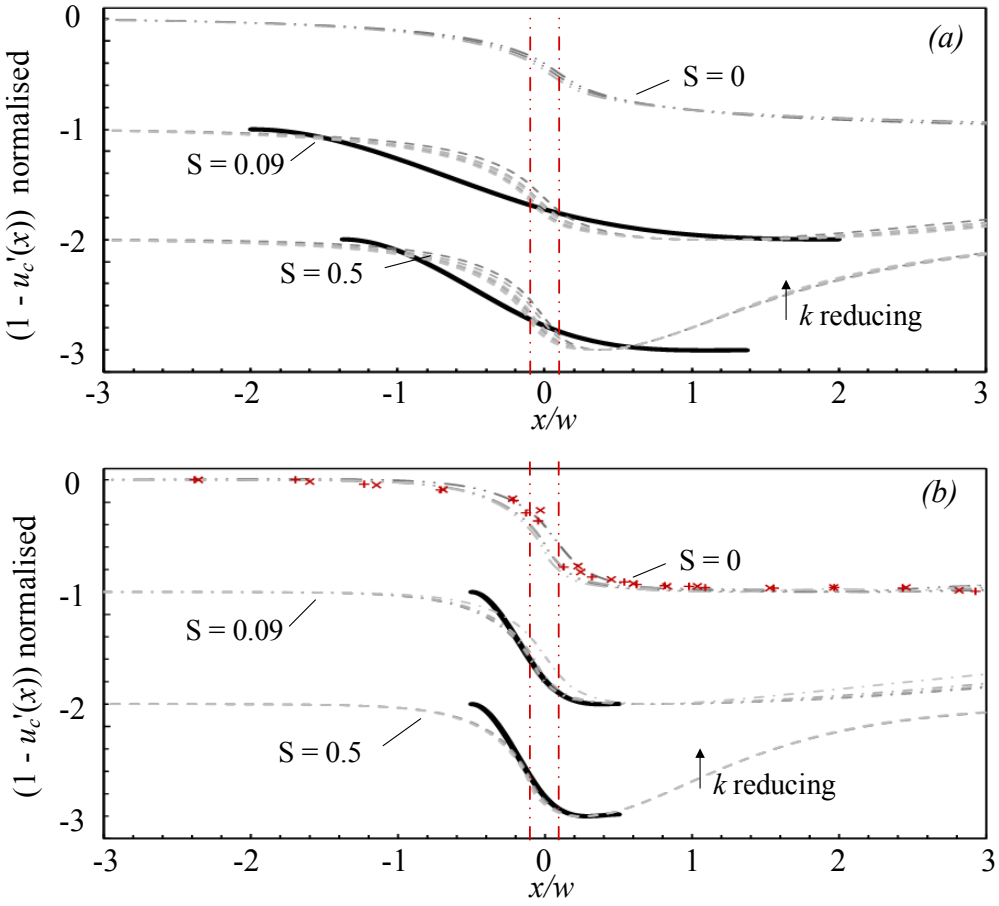

Figure 3. Normalised core flow velocity, $(1 - u_c'(x'))/(\min(u_c'(x')) - 1)$, profiles from the numerical simulations (dashed, dashed-dot lines) for a range of k values at $S = 0$, 0.09 and 0.5; *(a)* $B = 0.05$, $k = 1$–35 and *(b)* $B = 0.5$, $k = 2$–32. Also included in *(b)* are normalised core flow profiles for $S \approx 0$, $B = 0.35$, $k \approx 4$, digitised from the laboratory-based data of Zong and Nepf (2011, red +) and Chen *et al*. (2011, red x). The velocity is normalised using the minimum wake velocity for each scenario. Solid black lines are obtained using the theoretical model presented in §2 combined with equation (3.10). Red dashed-dot lines indicate upstream and downstream faces of the obstacle. For each increasing S value, the profiles have been displaced vertically by -1.

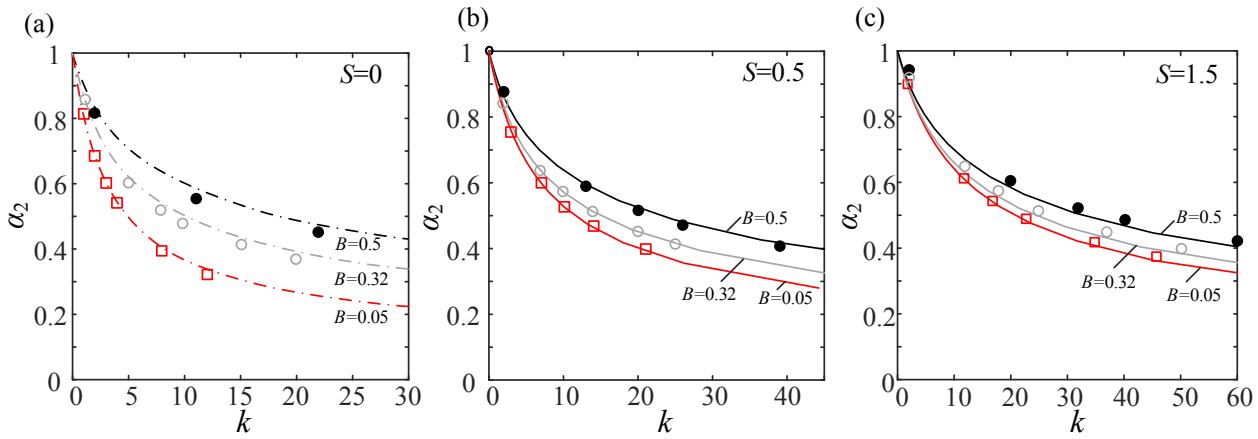

Figure 4: Variation in core flow velocity as a function of obstacle resistance k. (a) $S = 0$; (b) $S = 0.5$; (c) $S = 1.5$. Numerical results for $B = 0.05$ (open squares □); $B = 0.32$ (open circles ○) and $B = 0.5$ (solid circles ●). Solid lines are predictions using the theoretical model introduced in section 2 and fitted values of L'. Dashed lines are predictions that are equivalent to those obtained using the model due to Garrett and Cummins (2007). L' values used for (b) and (c) are obtained from figure 5.

To compare the theoretical model more directly with the numerical simulations, and to enable estimates of the length scales L'_u and L'_d, it is useful to quantify the core flow velocity passing through the obstacle in the simulations as

$$u_l = \alpha_2 U = \frac{1}{w} \int_{-w/2}^{w/2} u(0, y) dy. \tag{3.9}$$

where the centre of the obstacle is assumed to be at $(x, y) = (0,0)$. Having evaluated the core flow velocity coefficient α_2 for the numerical simulations in this way, it is now possible for each simulation (with a given k, B and S) to tune the length scales in the theoretical model to match the velocity coefficient. To simplify this tuning process it has been assumed that $L'_u = L'_d$; this represents a pragmatic assumption (and ultimately leads via equation (3.10) to an empirical result for these length scales that may be used to provide robust estimates of the core flow velocity for different input values of k, S and B).

Figure 4 presents some example fits to the numerical simulations for various combinations of blockage ratio, stability and resistance. Each line in this figure represents the theoretical model result with one fitted length scale $L' = 2L'_u = 2L'_d$. From these results it can be seen that a single length scale is sufficient across a range of obstacle resistance for a given blockage ratio and stability number; i.e. $L' = f(B, S)$. This is a convenient result which, in physical terms, indicates that the length over which the flow field diverges around the obstacle is less sensitive to k than to S or B, as might be anticipated (at least for low blockage ratio) from scale analysis presented by Rominger and Nepf (2011) for the upstream adjustment length.

To explore the functional form of L', the fitted length scales for all combinations of blockage ratio and stability number simulated numerically are presented in figure 5. Several comments can be made concerning the trends in these results. Firstly, for small values of S it can be seen that the fitted length scale increases as the blockage ratio reduces. This trend is consistent with the expectation that increased blockage tends to inhibit the divergence of streamlines, and therefore reduces the length over which flow divergence occurs. Furthermore for small blockage and small S the length scale is on the order of the obstacle width (i.e. $L' \sim O(1)$) which is not inconsistent with the scale analysis of Rominger and Nepf (2011). Secondly, for larger values of S it can be seen that the fitted length scale still increases as

the blockage ratio reduces, but for a given blockage the length scale reduces as S increases. This implies that increased background friction reduces the length over which the flow diverges around the obstacle by an amount similar to the reduction in fitted length scale. However, it should be noted that as the stability number increases the bypass flow becomes more two-dimensional in this limit (see figure 3). Additionally, the theoretical model fails to account for that fact that the background friction acts to mix the bypass and core flow in the wake of the obstacle, altering the pressure in the wake. Because of these effects, when S is large the fitted length scales are no longer expected to be directly related to the physical length over which flow divergence occurs.

To quantify the trends in figure 5 the following empirical relationship has been fitted for the length scale:

$$L' = 2L'_U = 2L'_d = f_1 e^{f_2 B} \tag{3.10}$$

where

$$f_1(S) = 1.4S^2 - 3.9S + 4.9 \text{ and } f_2(S) = -0.46S^2 + 1.8S - 3.2 \tag{3.11}$$

Equation (3.10) may be used directly with the theoretical model developed in Section 2 to predict the core flow velocity for any value of stability number and blockage ratio within the parameter space covered in this paper (i.e. for $0.05 \leq B \leq 0.5, 0.09 \leq S \leq 1.5$). We also remark that whilst the result in (3.10) is empirical it has the important property that for small stability number the length scale remains finite for all blockage ratios. This is physically meaningful since the main assumptions of the theoretical model (i.e. uniform, smoothly-varying core and bypass flow) are consistent with the numerical solution for small stability number, and so the fitted length scale is expected to resemble the actual (finite) length over which flow diversion occurs upstream and downstream of the obstacle.

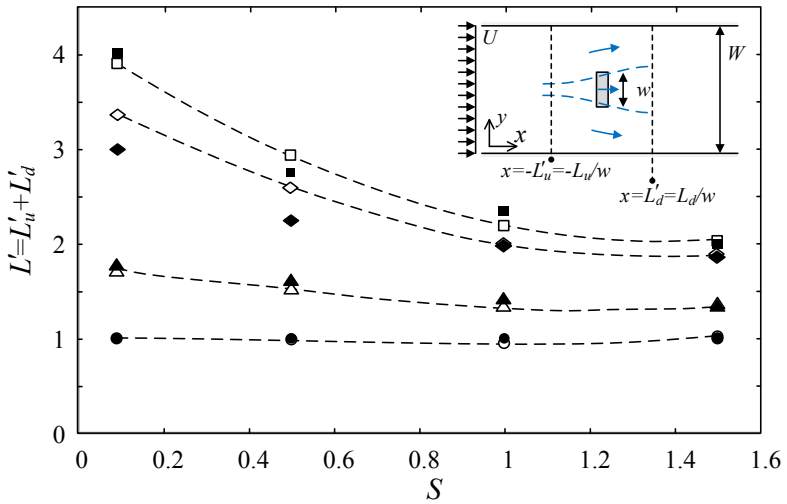

Figure 5. Variation in fitted length scale as a function of stability number and channel blockage ratio; $B = 0.5$ (circles ●), $B = 0.32$ (triangles▲), $B = 0.1$ (diamonds ♦) and $B = 0.05$ (squares ■). Lengths calculated using equation (3.10), dashed lines for $B = 0.5$ (open circles ○), $B = 0.32$ (open triangles Δ), $B = 0.1$ (open diamonds ◊) and $B = 0.05$ (open squares □).

In the following section we use the theoretical model (with the length scales defined by (3.10)) to provide new insight into two example problems that may be modelled according to the simplified problem geometry in figure 1.

4. Example applications

4.1 Prediction of core flow velocity through an array of emergent cylinders

Ball *et al.* (1996), Zong and Nepf (2011) and Chen *et al.* (2012) carried out laboratory experiments to analyse the bulk flow characteristics and wake structure associated with a compact porous obstacle represented as an array of emergent circular rigid cylinders. Apart from the work of Ball *et al.*, the motivation of this work was to better understand shallow water flows through aquatic vegetation, and the influence of flow diversion and wake dynamics on sediment and nutrient transport, bed morphology and water quality. Collectively, these studies explored a range of obstacle porosities (achieved by changing the number and spacing of cylinders), as well as a range of obstacle widths (so as to give blockage ratios spanning between 0.05 and 0.35) and different obstacle shapes (circle, square or rectangle). There were also slight variations in the stability parameter between the experiments, but S was generally below 0.04.

Figure 6 (a) presents experimental measurements reported by Zong and Nepf (2011), Chen *et al* (2011), and Ball *et al.* (1996) for the normalised velocity in the near wake of the obstacle (defined herein as α_4) as a function of obstacle resistance. In this figure the obstacle resistance k has been computed using equation (3.6), which requires an estimate for the pile drag coefficient, c_D. Zong and Nepf (2011) and Ball *et al.* (1996) assumed $c_D = 1$ for simplicity, whilst Chen *et al.* (2012) estimated c_D for each pile arrangement by assuming that the local drag is proportional to the solid volume fraction ϕ of the array (Tanino and Nepf, 2008). All of the experimental results plotted in figure 6 (a) are for configurations where $\phi < 0.15$. Within this range, Chen *et al*. calculated $1 < c_D < \sim 2$. For simplicity, we have chosen the average value, $c_D = 1.5$ to estimate k for all of the experimental values shown in figure 6 (a). For example, in one experiment of Zong and Nepf (2011), $l = D = 22$ cm, $\phi = 0.1$, $d = 0.64$ cm. Letting $c_D = 1.5$, equation (3.6) yields $k = 7.29$. Figure 6 (a) also shows the predictive formula adopted by Zong and Nepf (2011). This predictive formula, which is based on scaling arguments given in Rominger and Nepf (2011), assumes that the flow is able to adjust to the obstacle over its length, in which case the velocity is set by a momentum balance between the pressure gradient and the obstacle resistance at the downstream end of the obstacle. To contrast with the predictive formula of Rominger and Nepf (2011), Figure 6 (b) shows the same laboratory measurements as in figure 6 (b) but includes predictions based on the theoretical model presented in §2 (with S = 0.015; the mean value of the laboratory-based studies). Focusing initially on the experimental measurements, it can be seen in figure 6 (a) that there is a general reduction in magnitude of the near wake velocity as the obstacle resistance increases. At large resistance (i.e. $k > \sim$4-14, depending on channel blockage), this reduction appears to be captured properly by the predictive formula used by Zong and Nepf (2011). However, for low porosity it is difficult to determine a representative near wake velocity (see figure 4b in Zong and Nepf, 2011, for example), and this introduces some uncertainty into the comparison between Zong and Nepf's prediction and the experimental results in figure 6 for $k > 4$. In contrast, for lower resistance (i.e. more porous obstacles, $k <$ 4-14) the Zong and Nepf (2011) model gives a poorer prediction with the measurements, whilst the present theoretical model provides good agreement with the measurements, seen in figure 6 (b). In particular, much of the scatter in the laboratory data at lower resistance appears to be explained, according to the present theoretical model, by the blockage ratio used in the experiments (figure 6 b). Moreover, the normalised core flow velocity profiles from numerical simulations are in excellent agreement with the experimental results for very porous obstacles, seen in figure 3(b). In terms of predicting the flow through porous obstacles, the present theoretical model therefore appears to complement the model adopted by Zong and Nepf (2011), with the present model providing better predictions for very porous obstacles.

The maximum resistance (or minimum porosity) at which the obstacle transitions from being very porous (such that wake velocity no longer agrees with the present theoretical model) appears to be a function of blockage ratio. For instance, as indicated in figure 6 (b), the maximum resistance is between $k = 2$ - 4 for $B = 0.1$, $k = 3.5$ - 7.5 for $B = 0.18$ and $k = 4$ - 14 for $B = 0.35$. This suggests that the channel blockage ratio may be an important parameter both in controlling the core flow velocity through a very porous obstacle and in determining the limiting resistance at which the obstacle starts to behave as a low porosity obstacle.

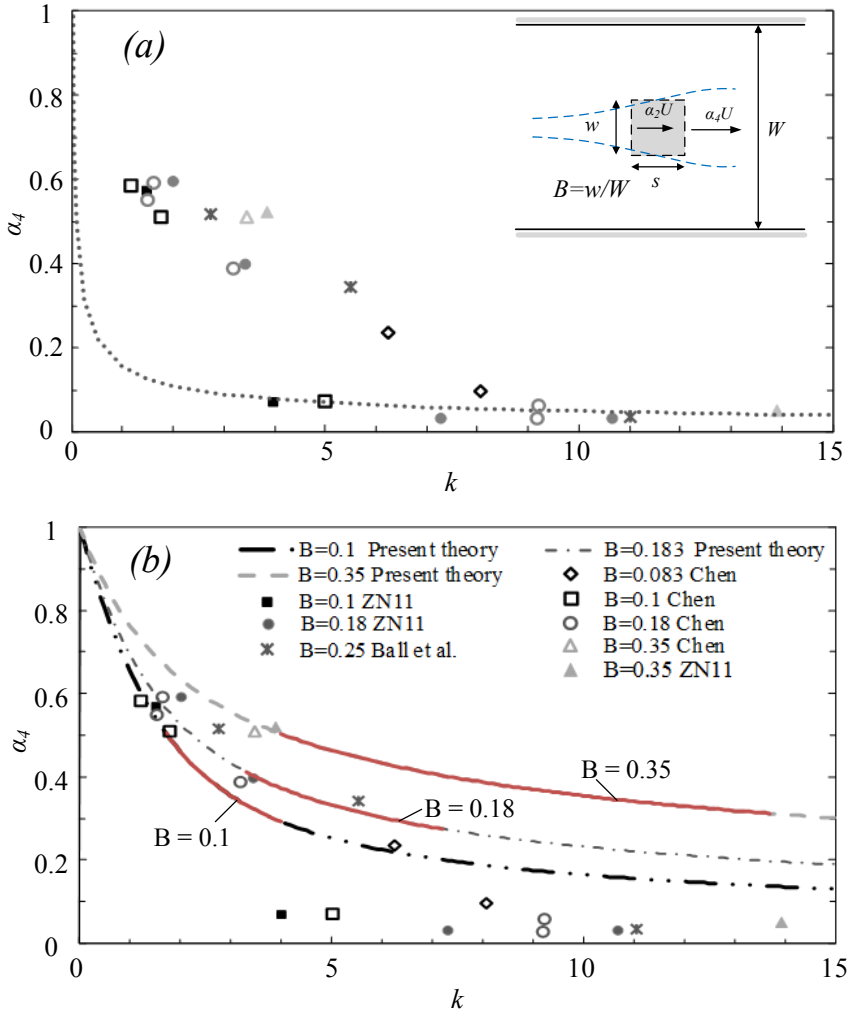

Figure 6: Variation of α_4 with k for experiments of Zong and Nepf (2011, ZN11; $B = 0.1$ solid squares, $B = 0.18$ solid circles, $B = 0.35$ solid triangles), Chen *et al.* (2012, $B = 0.083$ open diamonds, $B = 0.1$ open squares, $B \approx 0.18$ open circles, $B = 0.35$ open triangles) and Ball *et al.* (1996, $B = 0.25$, black stars) with; *(a)* theoretical model adopted by Zong and Nepf (2011, dotted line, S=0.019, $A_R = 1$); and *(b)* present theoretical model ($S = 0.015$; $B = 0.1$ dashed double dot, $B = 0.18$ dashed dot, $B = 0.35$ dashed). Solid red lines in *(b)* indicate the range in which the experimental results begin to deviate from the theoretical model.

The exact reason why the present theoretical model begins to over-predict the near wake velocity as the resistance of the obstacle becomes larger cannot be directly explained from the experimental results given in figure 6. However, it is relevant to note from figure 4 that the present model gives predictions in agreement with numerical simulations of the shallow water equations up to resistance values exceeding the threshold k values indicated above. Consequently, the maximum obstacle resistance at which the theoretical model starts to over-predict the measurements in figure 6 (b) coincides with the maximum resistance for which the depth-averaged shallow water simulations over-predict the measurements. In this sense, the results in figure 6 therefore highlight a limitation in the shallow water

equations for modelling the wake behind an obstacle with low porosity, and predicting accurately the flow velocity through the obstacle. This is consistent with previously identified limitations of the shallow water equations to reproduce the wake behind a porous obstacle and the velocity profile through the obstacle in shallow water (Ball *et al.*, 1996). In their study, Ball *et al.* modified the drag coefficient of the obstacle in order to obtain agreement with the experimental results. As the spacing between the cylinders reduced, i.e. as k increased, the ratio between the experimental and numerical drag coefficients increased. Ball *et al.* attributed this to the lack of horizontal diffusion in the shallow water model. For example, for an experimental $k = 2.76$, the numerical model requires $C_D = 1.9$, but for $k = 11$, $C_D = 5.6$ is required. The results presented in figure 6 confirm that the simple shallow water model and the theoretical model derived herein can be used to simulate accurately the hydrodynamics through and around a porous obstacle, provided it is sufficiently porous.

5.2 Optimum arrangements of tidal turbines in a channel

It is also possible to use the new theoretical model to explore quantitatively how natural seabed resistance may affect the optimum local spacing of tidal stream turbines in a channel. To do this one can follow the approach mapped out by Nishino and Willden (2012), who introduced the idea of scale separation to model a 'fence' of turbines partially blocking a wide channel (see figure 7). Nishino and Willden's approach was to model individual turbines within the fence as individual compact obstacles using the same theory as in §2 (but with $S = 0$) so as to compute the flow through each turbine as a function of a local geometric blockage B_l and resistance k_l (i.e. to obtain the local velocity coefficients $\alpha_{2,l}(B_l, k_l)$). At this 'turbine' scale the local blockage B_l was set equal to $A_t/(s+d)h_0$, in which A_t is the swept area of the turbine, d is the turbine diameter, and s is the spacing between adjacent turbines. The power extracted by each turbine was then computed as

$$P_l = \alpha_{2,l} U_l T = \frac{1}{2}\rho k_l \alpha_{2,l}^3 A_t U_l^3. \tag{4.1}$$

where U_l is the local upstream velocity.

To account for the fact that the collection of turbines also acts like a porous obstacle, Nishino and Willden (2012) also modelled the fence of turbines as an obstacle. At this 'array' scale the array blockage B_a was calculated as the ratio of fence area $A_f = N(s+d)h_0$, where N is the total number of turbines, to the cross-sectional area of the tidal channel. The array scale resistance was chosen to ensure the total force at array scale was equal to N times the force at local scale (i.e. the array and turbine scales were coupled by matching the force). This was achieved by setting the local resistance equal to $k_a = {\alpha_{2,l}}^2 k_l B_l$. The solution for the bulk flow velocity at this array scale was then used to calculate the local velocity, which is equal to $U_l = \alpha_{2,a} U$. Consequently, the total power removed from the channel was calculated according to

$$P = N\alpha_{2,l} U_l T = \frac{1}{2}\rho N k_l \alpha_{2,l}^3 A_t \left(\alpha_{2,a} U\right)^3. \tag{4.2}$$

Using this approach Nishino and Willden (2012) found that for a given array blockage, there was always an optimum local blockage B_L (i.e. an optimum arrangement of turbines) to maximise power. Furthermore, they showed that this optimum result agreed reasonably well with 3D numerical simulations of long fences of porous obstacles emulating turbines (Nishino and Willden, 2013).

Despite obtaining reasonable agreement with 3D numerical simulations, a limitation of the Nishino and Willden (2012) analysis was that the tidal channel was assumed to be frictionless. In reality, however, a fence of turbines could span over a width $w \sim O(10^3)$ m. Thus, taking $C_d \sim O(10^{-3})$ and $h_0 \sim O(10^1)$ m, it follows that at the array scale $S \sim O(10^{-1})$ and so frictional effects may not be negligible. Motivated by this result, the theoretical model developed in §2 is used in this section to

update the model presented by Nishino and Willden (2012). This is achieved by using the theoretical model presented in §2 to model the fence at 'array' scale, whilst maintaining the frictionless solution at 'local' scale (where frictional forces are likely to be less important relative to the force provided by the turbines, *i.e.* the local length scale is expected to be a small fraction of the array length scale). To provide an example solution, $B_a = 0.05$ is assumed. This represents a very wide channel, in which the net resistance of the tidal turbines is unlikely to have a back effect on the net flow through the channel (Vennell, 2010).

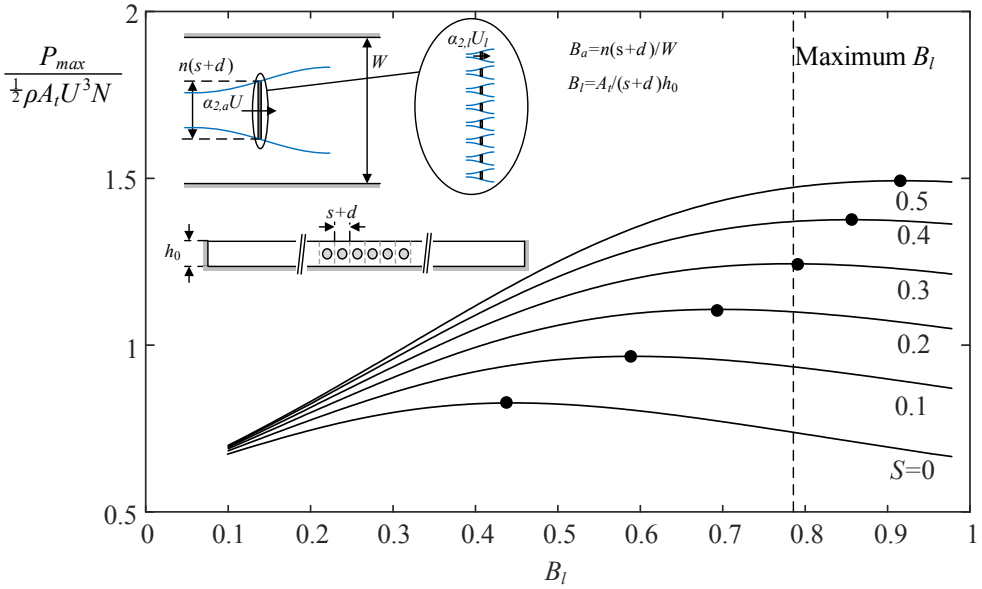

Figure 7: Maximum power as a function of local blockage for a fence of turbines having a total length equal to 5 % of the channel width (i.e. $B_a = 0.05$). Vertical dashed line indicates the maximum local blockage ratio for circular turbines. Dots indicate the optimum local blockage ratio; i.e. the optimum local spacing/arrangement of turbines within the fence for a given stability number.

Results are presented in figure 7 for maximum power, as a function of B_l, for different values of stability number. It can be seen that there is a substantial increase in power generation as S increases. For example, regardless of local blockage ratio, the values of C_P increase compared to the frictionless result. This increase occurs simply because background friction acts to resist the faster moving bypass flow and force more flow through the fence. Consequently turbines can provide greater resistance and remove more power before a significant fraction of the flow starts to bypass the fence. Figure 7 also shows that the optimum local blockage increases with stability number; indicating that it is advantageous to place turbines closer together in frictional tidal channels. This increase is such that for $S > \sim 0.3$ the optimum blockage exceeds $\pi/4 \sim 0.78$, which is the largest local blockage for circular turbines in a rectangular channel. In such instances, the model therefore indicates that the turbines should be placed as close as practically possible to generate more power.

In terms of the validity of these estimates it should be noted that for optimum power extraction and optimum turbine arrangement (indicated by the dots in figure 7) the resistance of the array is $k_a = 1.0$ and $k_l = 4.9$ when $S = 0$. Noting that $B_a = 0.05$ and $B_l = 0.44$, these resistances appear to be within the very porous range identified in §4.1 for similar blockage ratios; thus validating the use of the underlying theoretical models. For larger values of S the results in §4.1 cannot be used to infer whether the turbines still represent very porous obstacles. It would be insightful to investigate if this is the case in future work.

5. Conclusions

A theoretical model has been developed to predict the core flow velocity passing through a compact porous obstacle in a shallow channel. This model extends the model of Garrett and Cummins (2007) to include natural bed resistance and is applicable to the prediction of flow through emergent aquatic vegetation, the performance of arrays of stream turbines in tidal channels, and the net forces on offshore structures. The new model is particularly relevant when combined effects of stability number S, channel blockage B and porosity (or obstacle resistance k) are important.

Direct application of the theoretical model to arrays of emergent cylinders emulating a patch of aquatic vegetation has indicated that the model provides satisfactory predictions of core flow velocity over the range for which the shallow water equations are valid. Within this range (i.e. for very porous obstacles) the present model indicates that channel blockage ratio has a noticeable effect on the core flow velocity, even at small values of blockage ratio. As a consequence, the channel blockage ratio should be considered when interpreting and developing predictive formulae based on laboratory data measured in confined flumes and channels. One application of the new theoretical model could therefore be the optimisation of future laboratory experiments involving arrangements of aquatic vegetation. A second application could include combining the present model with predictive models of wake dynamics, such as wake length and wake mixing, which require core flow velocity as a primary input.

The theoretical model proposed herein has also been used to confirm that, for a given flow velocity, the existence of natural bed resistance (i.e. $S > 0$) enables greater power extraction from turbines arranged in a partial fence within a very wide channel. Natural bed resistance has been shown to influence the optimum arrangement of turbines in the fence in this case. For $S > \sim 0.3$, the model indicates that turbines placed in a fence should be spaced as close together as is practically possible for maximum power extraction. For $S \leq \sim 0.3$, there is an optimum spacing between turbines to remove maximum power. Similar insights might also be gained by using the proposed model to explore optimum arrangements of turbines. For example, the model may be used to extend further the analysis presented for staggered and centred arrays of turbines by Draper and Nishino (2014).

Through comparison of the proposed theoretical model with experimental data it was found that there exists a minimum porosity below which the present theoretical model and the shallow water approximation of flow through a porous obstacle become invalid. This minimum porosity is a function of the blockage ratio. However, whilst the comparison provided an indication of the limiting porosity for small stability number, further experimental data are required, particularly for high blockage ratios and higher natural bed resistance, to better describe this limitation. These results will be of particular importance in the prediction of shallow water flows through and around aquatic vegetation, tidal turbine arrays, and geometrically porous offshore structures.

Data Accessibility

This paper has no experimental data.

Competing Interests

We have no competing interests.

Authors' contributions

Theoretical concept developed by T.N. and S.D. Theoretical and numerical modelling was carried out jointly by M.C. and S.D. All authors' contributed to the data analysis and writing of the paper.

Acknowledgments

The first author would like to acknowledge generous support from the Royal Society of Edinburgh through a Lessells Travel Scholarship. The second author would like to acknowledge kind support from

the Lloyd's Register Foundation. Lloyd's Register Foundation invests in science, engineering and technology for public benefit, worldwide.

Funding Statement

This work was supported by the Royal Society of Edinburgh Lessells Travel Scholarship and the Llyod's Register Foundation.

References

BALL, D.J., STANSBY, P.K. & ALLISTON, N., 1996. Modelling shallow water flow around pile groups. *Proceedings of the Institution of Civil Engineers. Water, Maritime and Energy*, **118**(4):.226-236.

CHEN, D. & JIRKA, G. H., 1995. Experimental study of plane turbulent wakes in a shallow water layer. *Fluid Dynamics Research*, **16**(1): 11-41.

CHEN, Z., ORTIZ, A., ZONG, L. & NEPF, H., 2012. The wake structure behind a porous obstruction and its implications for deposition near a finite patch of emergent vegetation. *Water Resources Research*, **48**, W09517.

DRAPER, S. & NISHINO, T., 2014. Centred and staggered arrangements of tidal turbines. *Journal of Fluid Mechanics*, **739**: 72-93.

HOULSBY, G.T., DRAPER, S. & Oldfield M.L.G., 2008. Application of linear momentum actuator disc theory to open channel flow. *Tech. Rep.* OUEL, 2296(08), University of Oxford.

JACKSON, G.A., 1997. Currents in the high drag environment of a coastal kelp stand off California. *Continental Shelf Research*, **17**(15): 1913-1928.

GARRETT, C. & CUMMINS, P., 2007. The efficiency of a turbine in a tidal channel. *Journal of Fluid Mechanics*, **588**: 243-251.

GARRETT, C. & CUMMINS, P., 2013. Maximum power from a turbine farm in shallow water. *Journal of Fluid Mechanics*, **714**: 634-643.

MAZDA, Y., WOLANSKI, E., KING, B., SASE, A., OHTSUKA, D., & MAGI, M., 1997. Drag force due to vegetation in mangrove swamps. *Mangroves and Salt Marshes*, *1*(3), 193-199.

NICOLLE, A. & EAMES, I., 2011. Numerical study of flow through and around a circular array of cylinders. *Journal of Fluid Mechanics*, **679**: 1-31.

NISHINO, T. & WILLDEN, R.H.J., 2012. The efficiency of an array of tidal turbines partially blocking a wide channel. *Journal of Fluid Mechanics*, **708**: 596-606.

NISHINO, T. & WILLDEN, R.H.J., 2013. Two-scale dynamics of flow past a partial cross-stream array of tidal turbines. *Journal of Fluid Mechanics*, **730**: 220-244.

ROMINGER, J.T. & NEPF, H.M., 2011. Flow adjustment and interior flow associated with a rectangular porous obstruction. *Journal of Fluid Mechanics*, **680**: 636-659.

SOARES-FRAZÃO, S., LHOMME, J., GUINOT, V. & ZECH, Y., 2008. Two-dimensional shallow-water model with porosity for urban flood modelling. *Journal of Hydraulic Research*, **46**(1): 45-64.

STANSBY, P.K., 2003. A mixing-length model for shallow turbulent wakes. *Journal of Fluid Mechanics*, **495**: 369-384.

STANSBY, P.K., 2006. Limitations of depth-averaged modelling for shallow wakes. *Journal of Hydraulic Engineering*, **132**(7), pp.737-740.

TAKEMURA, T. & TANAKA, N., 2007. Flow structures and drag characteristics of a colony-type emergent roughness model mounted on a flat plate in uniform flow. *Fluid Dynamics Research*, **39**(9): 694-710.

TORO, E.F., SPRUCE, M. & SPEARES, W., 1994. Restoration of the contact surface in the HLL-Riemann solver. *Shock waves*, **4**(1): 25-34.

VENNELL, R., 2010. Tuning turbines in a tidal channel. *Journal of Fluid Mechanics*, **663**: 253-267.

WOOD, C.J., 1964. The effect of base bleed on a periodic wake (Airfoil drag reduction via base bleeding and vortex street strength decrease). *Royal Aeronautical Society, Journal*, **68**: 477-482.

ZONG, L. & NEPF, H., 2012. Vortex development behind a finite porous obstruction in a channel. *Journal of Fluid Mechanics*, **691**: 368-391

Appendix

A cubic spline has been used to describe the streamwise variation in core flow velocity. To form the spline, piecewise cubic polynomials have been defined on the intervals $x' \in (-L'_u, 0)$ and $x' \in (0, L'_d)$. The first and second derivatives of these functions have been set equal at $x' = 0$; i.e.

$$u_c(-L'_u) = U;\ \ u_c(0) = \alpha_2 U;\ \ u_c(L'_d) = \alpha_4 U; \tag{A.1}$$

and

$$\frac{d}{dx'}\big(u_c(-L'_u)\big) = \frac{d}{dx'}\big(u_c(L'_d)\big) = 0. \tag{A.2}$$

This leads to

$$\frac{u_c}{U} = \begin{cases} a_1(x' + L'_u)^3 + b_1(x' + L'_u)^2 + 1; & -L'_u < x' < 0 \\ a_2(x' - L'_d)^3 + b_2(x' - L'_d)^2 + \alpha_4; & 0 < x' < L'_d \end{cases}, \tag{A.3}$$

where

$$a_1 = -3\,\frac{(\alpha_2 - \alpha_4)}{2(L'_u L'^2_d + L'_d L'^2_u)} - \frac{(\alpha_2 - 1)(L'_d + 4L'_u)}{2L'^2_u(L'^2_u + L'_d L'_u)}, \tag{A.4}$$

$$a_2 = \ 3\,\frac{(\alpha_2 - 1)}{2(L'_d L'^2_u + L'_u L'^2_d)} - \frac{(\alpha_2 - \alpha_4)(L'_u + 4L'_d)}{2L'^2_d(L'^2_d + L'_u L'_d)}, \tag{A.5}$$

$$b_1 = 3\,\frac{(\alpha_2 - \alpha_4)}{2(L'^2_d + L'_d L'_u)} + 3\,\frac{(\alpha_2 - 1)(L'_d + 2L'_u)}{2L'_u(L'^2_u + L'_d L'_u)}, \tag{A.6}$$

and

$$b_2 = \ 3\,\frac{(\alpha_2 - 1)}{2(L'^2_u + L'_u L'_d)} + 3\,\frac{(\alpha_2 - \alpha_4)(L'_u + 2L'_d)}{2L'_d(L'^2_d + L'_u L'_d)}. \tag{A.7}$$

From continuity it then follows that the width of the core flow, w_c, and the width of the bypass flow, w_b, satisfy

$$\frac{w_c}{w} = \frac{\alpha_2 U}{u_c}, \quad \frac{w_b}{w} = \frac{1}{B} - \frac{w_c}{w}. \tag{A.8}$$

Hence the bypass flow velocity may be evaluated as

$$\frac{u_b}{U} = \frac{w}{w_b}\left(\frac{1}{B} - \alpha_2\right). \tag{A.9}$$